Computer Methods in Biomechanics and Biomedical Engineering, Vol. 2, pp. 83–105
Reprints available directly from the publisher
Photocopying permitted by license only

Fibre Orientation in Human Fetal Heart and Ventricular Mechanics : A Small Perturbation Analysis

J. OHAYON[a,*], Y. USSON[b], P. S. JOUK[c] and H. CAI[d]

[a]*Department of Composite Material, LaMaCo, Engineering School of Chambery, University of Savoie, 73376 Le Bourget du Lac, France;* [b]*Laboratoire TIMC, Institut Albert Bonniot, Université Joseph Fourier, Domaine de la Merci, 38706 La Tronche Cedex, France;* [c]*Fédération Génétique Reproduction Développement, Centre Hospitalier Universitaire de Grenoble, Université Joseph Fourier, BP 217, 38043 Grenoble Cedex 9, France;* [d]*Department of Composite Material, LaMaCo, Engineering School of Chambery, University of Savoie, 73376 Le Bourget du Lac, France*

(Received 30 January 1997; Revised 19 June 1998)

The study of the topological organisation of myocardial cells is a basic requirement for understanding the mechanical design of the normal and pathological heart. Anatomical observations show that cardiac muscle tissue has a highly specialized architecture. We have made new quantitative measurements of fibre orientation through the heart wall by means of polarized light analysis on some thick sections of human fetal heart embedded in a resin and polymerized. A small perturbation method to find an equilibrium solution in a cylindrical left ventricular (LV) geometry with fibres running on toroidal shells of revolution is used to investigate the mechanical behaviour of three human fetal hearts (FH) of 14, 20 and 33 weeks of gestational age.

The results of fibre strains and stresses presented for end-systolic state show significant differences when compared to results of the cylindrical geometry with regular helicoidal fibres running on cylindrical surfaces. Moreover, the toroidal shells of revolution explain shear stresses and strains in the transverse plane which also exist in the adult heart.

Keywords: Myocardial fibre orientation, myocardial strains, myocardial stresses, human fetus, mathematical model, perturbation methods

1. INTRODUCTION

Cardiac muscle tissue, or myocardium, is a complex structure composed primarily of cardiac muscle cells arranged in a more or less parallel weave. Each cell has several branches to other cells, but nonetheless a sense of direction or grain is preserved. We shall denote the local grain direction by the unit vector $\underset{\sim}{\tau}$

*Corresponding Author: Tel: (33) 479 75 8604; Fax: (33) 479 75 8772; E-mail: ohayon@univ-savoie.fr

and refer to it also as the local "fibre" direction with the understanding that individual continuous muscle fibre do not really exist.

The anisotropic elastic behaviour of the left ventricle (LV) due to fibre orientation is now well recognized. A simple mathematical model of the mechanics of the left ventricle, which considers the main features of the highly specialized architecture of active muscle fibres, is necessary for a good description of cardiac performance.

Quantitative measurements of fibre orientation through the heart wall have been made on mature heart [1,2,3,4,5,6]. These results show: (i) a smooth transmural variation of fibre orientation, and (ii) that the myocardium is a continuum rather than an assembly of discrete fibre bundles. This pattern has been studied with four different approaches: mechanical peeling of the fibres of the total heart from epicardium to endocardium [1,2,3], study of macroscopical serial sections of the heart [4], histological study of a sampled region of myocardium of the ventricular wall [5], and more recently using the uniaxial light polarizing properties of the myocardial fibres on some thick sections of heart embedded in a resin and polymerized [6]. In this paper we use this last original approach to characterize the orientation of myocardial cells of three human fetal hearts (FH).

Several models currently exist that attempt to calculate the transmural distributions of stresses and strains as well as energetic quantities. Treating the myocardium as a fluid-fibre–collagen continuum has been successfully applied to the LV modeled as a finite thick–walled cylinder [7,8,9,10,11,12,13, 14,15,16], any general axisymmetric shapes that are small perturbations of a thick-walled finite cylinder [17], or more realistic geometry using Finite Element Analysis [18,19,20,21,22,23], but assuming that the muscle fibre are running from base to apex in planes parallel to the endocardial and epicardial surfaces. In this paper we present a small perturbation approach to find an equilibrium solution in a cylindrical LV geometry with fibre running on toroidal shells of revolution as obtained by assuming axial symmetry of the fibre orientation in the lateral wall of the fetal LV. Then simulations on the mechanical behaviour of the FH are performed and the effect of fibre orientation on myocardial strain and stress distributions is analyzed at end-systole.

2. MAPPING OF THE ORIENTATION OF MYOCARDIAL CELLS BY POLARIZED LIGHT MICROSCOPY

2.1 Materials and Methods

Human fetal tissue was obtained and processed in compliance with French legal and ethical guidelines. These nonviable embryos and fetuses, as define by the U.S. code of Federal Regulations, were obtained during legal terminations of pregnancy related to problems of maternal health.

Three human fetal hearts of 14, 20 and 33 weeks of gestational age (noted respectively FH14, FH20 and FH33) were fixed in a solution of 10% neutral buffered formalin by perfusion and immersed 1 week in the same solution. Then the hearts were embedded in a resin of methyl methacrylate. In order to have a constant anatomical reference for further orientation analysis, the hearts were maintained vertically during the polymerization process. For every heart, a series of thick sections (500 μm), transverse with reference to the base to apex axis, was cut with a rotatory microtome at a slow rate of penetration in order to avoid mechanical stress and distortions. The fibre orientation maps were generated by means of image analysis of polarized light microscopy. The myocardial fibres embedded in methylmetacrylate react between crossed-polarizers as a crystal whose indicatrix is positive, uniaxial with a zero degree extinction angle. In these conditions, the amount of transmitted light for a single fibre of known maximal birefringence is a function of the three-dimensional orientation of the axis of its indicatrix. The amount of monochromatic light that reaches the analyzer (upper polarizer) is given by the Fresnel's equation (in 24) and adapted by Johanssen [25]

$$\frac{I}{I_0} = \sin^2\left(\pi\frac{\nu}{\kappa}\right)\sin^2(2\delta) \qquad (1)$$

where ν and κ are the retardation and wavelength of the monochromatic light, respectively, δ is the angle between the direction of the fibre and the closest direction of either polarizer or analyzer, and I_0 is the intensity of light with no retardation. In practice we do not deal with a single fibre but with a tissue made of numerous fibres with different orientations that are to be measured. At a given *point P* (or voxel which is an elementary volume of 130 × 130 × 500 μm), the local grain orientation can be derived from two angles, the azimuth angle γ_{azi} and the elevation angle γ_{ele} with reference to the plane of the section (Figure 1). The azimuth angle γ_{azi} is defined as the angle between the projection of the fibre on the section plane and the x axis of the rectangular cartesian coordinates (x, y, z). The elevation angle γ_{ele} is the angle of the fibre with the section plane. These angles can be derived from ν and δ by means of multiparametric acquisition. Four images of the still object were acquired between a pair of cross-polarizing filters. The first setting (α_0) corresponded to an alignment of the vibration axis of the polarizer with the East-West axis of the microscope stage. The other three settings ($\alpha_{\pi/8}$, $\alpha_{\pi/4}$ and $\alpha_{3\pi/8}$) corresponded to incremental rotations of the pair of cross-polarizing lenses by an amount of $\pi/8$ radians. The angles γ_{azi} and γ_{ele} at each point of the myocardial section are obtained by combining the measurements ($L\alpha_0$, $L\alpha_{\pi/8}$, $L\alpha_{\pi/4}$ and $L\alpha_{3\pi/8}$) of the intensity of transmitted light at the corresponding pixels of the four images according to following formulas:

$$\gamma_{azi} = 0.25 \text{ Arg}((L\alpha_0 - L\alpha_{\pi/4}) + i(L\alpha_{3\pi/8} - L\alpha_{\pi/8})) \quad (2a)$$

$$\gamma_{ele} = \arccos\left(\frac{L\alpha_{max}}{L_{max}}\right)^{1/4} \quad (2b)$$

with $i^2 = -1$, Arg is the argument, $L\alpha_{max}$ the greatest of the four $L\alpha$ values and L_{max} the maximum intensity obtained for a fibre with $\gamma_{azi} = \pi/4$ and $\gamma_{ele} = 0$. However the range of γ_{azi} is limited to $\pi/2$ when using four images. We extended this range to π by adding a full wave-plate in the optical path and recording four additional images. This auxiliary plate makes it possible to discriminate the sign of the retardation in every pixel. The orientation maps obtained this way were validated by means of confocal microscopy [2,26]. The angular resolutions were, ±1° for the γ_{azi}, ±1° for the γ_{ele} in the range [10°, 60°] and ±5° elsewhere [6]. The reproducibility and accuracy of the measurements were

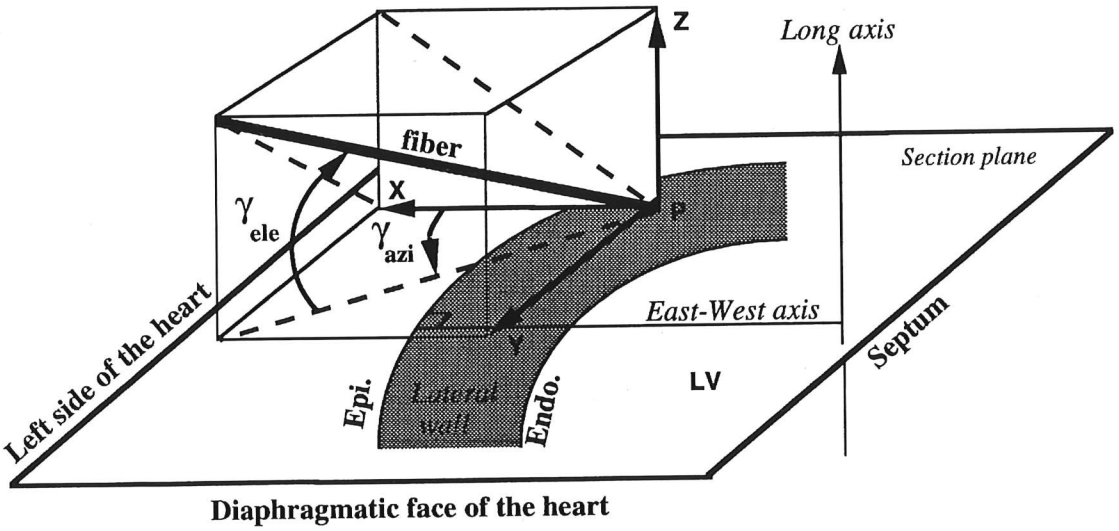

FIGURE 1 Definition of the angular reference system used for this study. Schematic view of a transverse cut showing the fibre orientation at a point *P* in the lateral wall. To define the fibre direction in a rectangular cartesian coordinates system (x, y, z), two angles are needed: the elevation angle γ_{ele} and the azimuth angle γ_{azi}. The dash lines are projections of the fibre on the xy, xz and yz planes. LV: left ventricle, Endo.: endocardium, Epi.: epicardium.

assessed by comparing them with those provided by confocal microscopy and were extensively discussed in [26]. With the present method the elevation angle γ_{ele} is known modulo 90°. This is the main limitation of the method which presently precludes giving a complete three-dimensional representation of the orientation of the indicatrix of the myocardium.

2.2 Orientation of Myocardial Cells in the Lateral Wall of the LV

The results presented in this paper concern three FH at different developmental stages. As such these data cannot yet be generalized to all human FH. However these three FH were chosen for analysis because from all our observations done on several FH at the same stages, they represent typical observations.

All the measurements are made on the East-West axis in the lateral wall of the fetal LV (Figure 1). Three kinds of maps (Figure 2) are presented in this study on the orientation of myocardial cells in the lateral wall of the LV. The two first kinds of maps are colour coded representations of γ_{ele} (Figure 2A) and γ_{azi} (Figure 2B). The third one, called the 3D orientation map (Figure 2C) is coded with linear segments for which the lengths are proportional to the square cosine of their elevation (γ_{ele}) and for which the planar orientations give the azimuth angle (γ_{azi}). Only every second point is shown in order not to overcrowd the figures. The last column (Figure 2D) represents a schematic interpretation of the fibre orientation in the transverse section.

Results on azimuth angle γ_{azi} in the lateral wall

The maps in Figure 2 correspond to three transverse sections of the lateral wall of the LV, near the base, equator and near the apex for the FH33. On the basal section if one considers the azimuth, the fibres run from endocardium to epicardium in an anti-clockwise twisted fashion. On the equatorial section the fibre follow perfectly the curvature of the ventricular wall, and on the apical section if one only considers the azimuth, the fibres run from endocardium to epicardium in a clockwise twisted fashion.

Because the measurements are made on the East-West axis in the lateral wall (arrow head, Figure 2C), where the angle between the tangent to the epicardial layer in the section plane and the y axis is close to zero (Figure 1), a transverse angle γ_{tra} as defined by Streeter [5] can be derived from the azimuth angle γ_{azi} ($\gamma_{tra} = \pi/2 - \gamma_{azi}$). The spatial distributions of the transverse angle γ_{tra} are given for the three FH in Figure 3. Prior observations, done on the transverse angle of the FH33 (Figure 3C), are also true for the FH20 (Figure 3B). For the FH14 the results are slightly different on the basal section where the fibres tend to follow the curvature of the ventricular wall as on the equatorial section (Figure 3A).

Results on elevation angle γ_{ele} in the lateral wall

For the three FH, the variation of the elevation fibre angle from the endocardial to the epicardial surfaces in the lateral wall are measured in each transverse section. Figure 2A shows that in the subendocardial and subepicardial layers the elevation angles are high which corresponds to fibres nearly parallel to the base-apex axis. In the central layers γ_{ele} is almost constant ($30° \leq \gamma_{ele} \leq 50°$) except for the very mid-wall region where the fibres are running inside the section thickness ($\gamma_{ele} \leq 30°$). It appears that, for a single FH, the variations between all measured distributions are small. The mean distribution of γ_{ele} for each FH is given in Figure 4A. Note that the three analyzed FH have similar distributions of the mean elevation angle in the lateral wall (Figure 4A).

From these observations we can extract four main anatomical features in the lateral wall of these three fetal LV.

The first one refers to the distribution of the elevation angle from endocardial to epicardial surfaces. In FH the observed variations of the distributions of the elevation angle from base to apex were small compared to those measured by Streeter [5] and Nielsen *et al.* [3] in adult hearts. Therefore we use a mean distribution of γ_{ele} (Figure 4A).

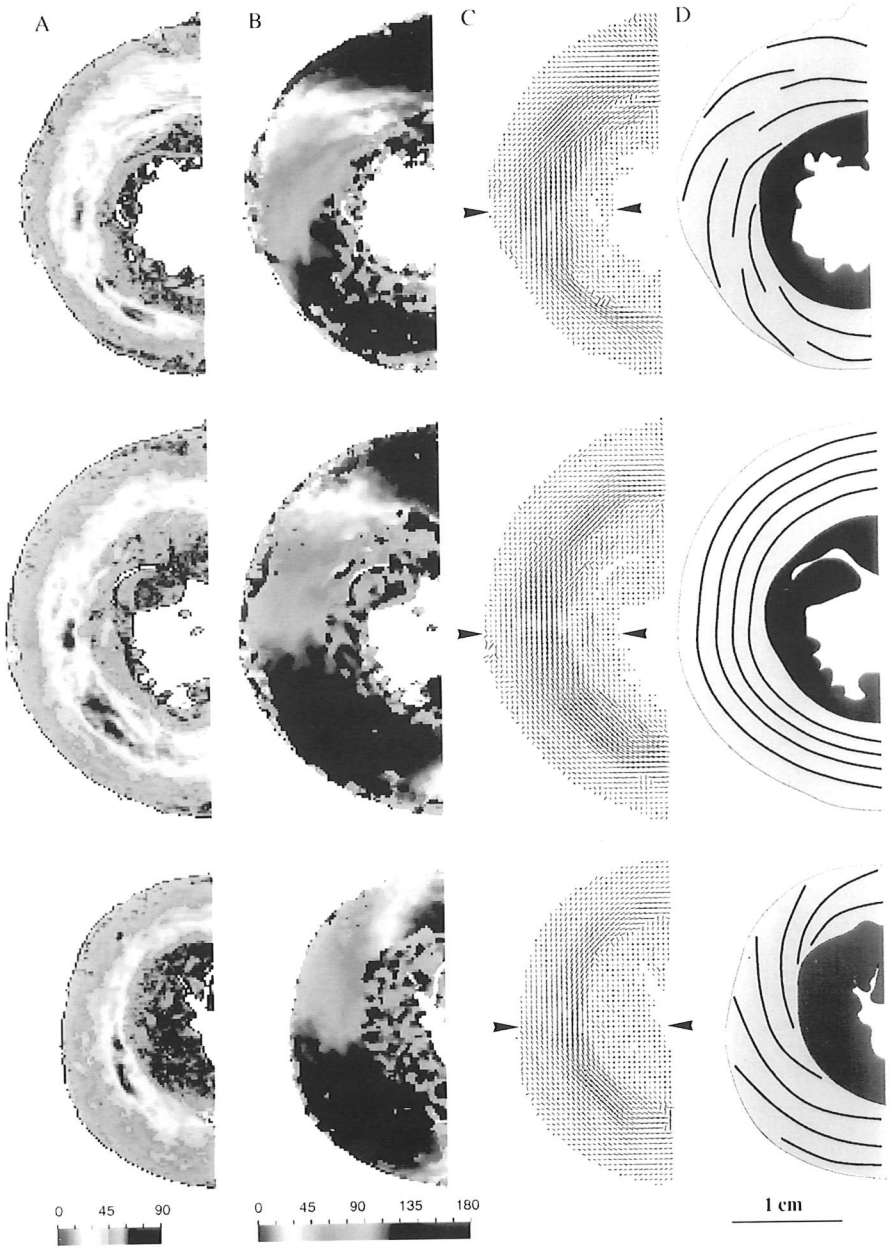

FIGURE 2 Measured fibre organization in the lateral wall of the left ventricle on three transversal sections at the base (Top maps), the equator (middle maps) and the apex (Bottom maps) of the fetal heart of 33 weeks of gestational age (FH33). **Column A:** Colour maps giving the spatial distributions of the elevation angle in the transversal sections (colour scale: $0° \leq \gamma_{ele} \leq 90°$). **Column B:** Colour maps giving the spatial distributions of the azimuth angle in the transversal sections (colour scale: $0° \leq \gamma_{azi} \leq 180°$). **Column C:** 3D maps of measured fibre orientation, the angle between the direction of a segment and the horizontal line indicates the azimuth angle, the length of a segment is proportional to the planar projection of the orientation vector. It is maximal for a circular fibre (fibre running in the plane of the map) and minimal for a fibre orthogonal to the plane (crosses correspond to fibre whose elevation is superior to 60°). Arrows indicate the East-West axis in the lateral wall where the measurements are made. **Column D:** schematic drawing of the bundles of fibres as interpreted from the orientation maps. In the basal section, the bundles seem to radiate from endocardium to epicardium in an anticlockwise twisted fashion. At the equator the fibres are mainly circular and seem to follow perfectly the bow of the ventricular wall. At the apex, the bundles of fibres seem to radiate from endocardium to epicardium in an clockwise twisted fashion. Scale bar : 1 cm. (See Colour Plate at back of issue.).

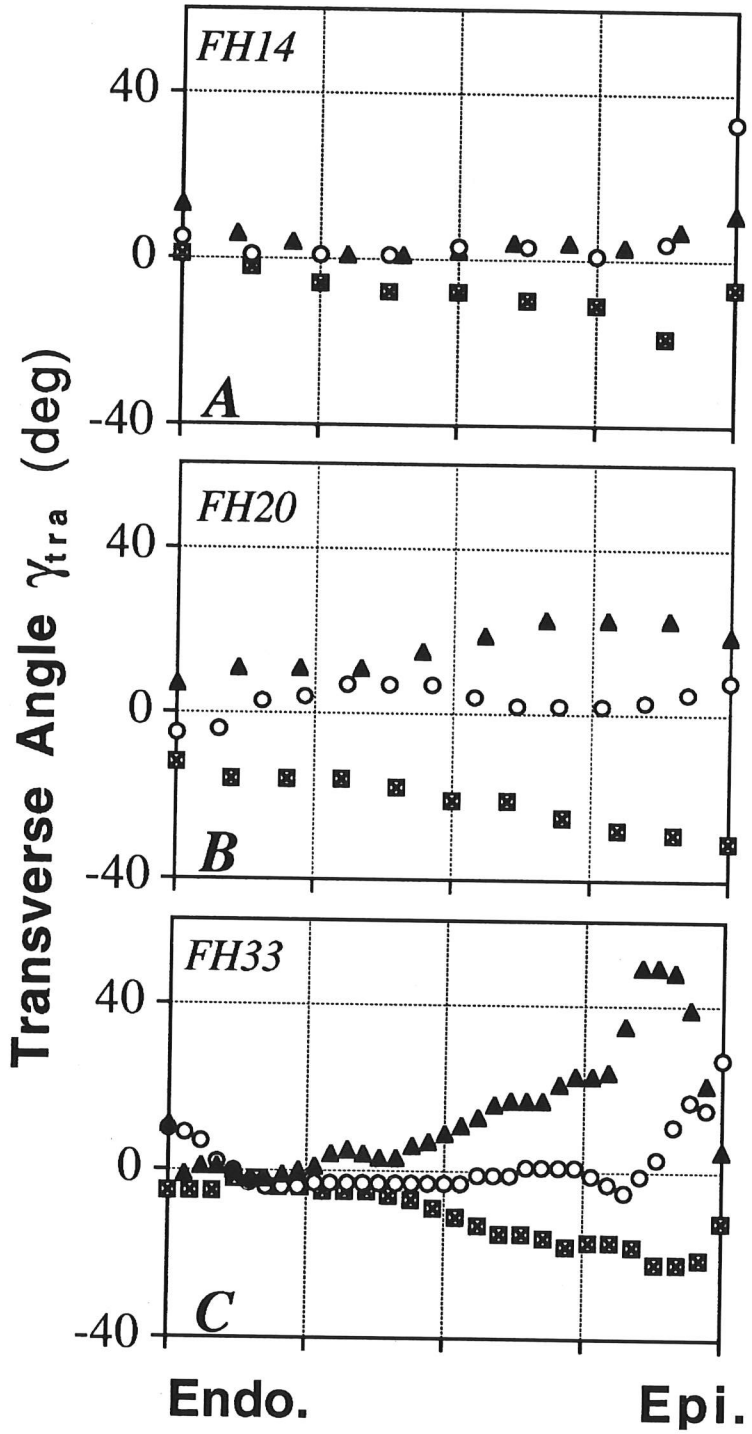

FIGURE 3 Measured spatial distributions of the transverse fibre angle γ_{tra} in the lateral wall of the left ventricle at the base (triangles), equator (circles) and apex (squares) for the fetal hearts of A) 14 weeks (FH14), B) 20 weeks (FH20), and C) 33 weeks (FH33) of gestational age. The Units of γ_{tra} are degrees. One must note the opposition of sign of γ_{tra} between base and apex, while it remains close to zero at equator.

The second one refers to the comparison of the mean distributions of the elevation angle from endocardial to epicardial surfaces between the FH14, FH20 and FH33. These distributions are almost the same (Figure 4).

The third one refers to the traversing of fibres from endocardium to epicardium. The transverse angle γ_{tra} is almost null at the equator and increases (positive angle) toward the base giving the anticlockwise twist previously described. The transverse

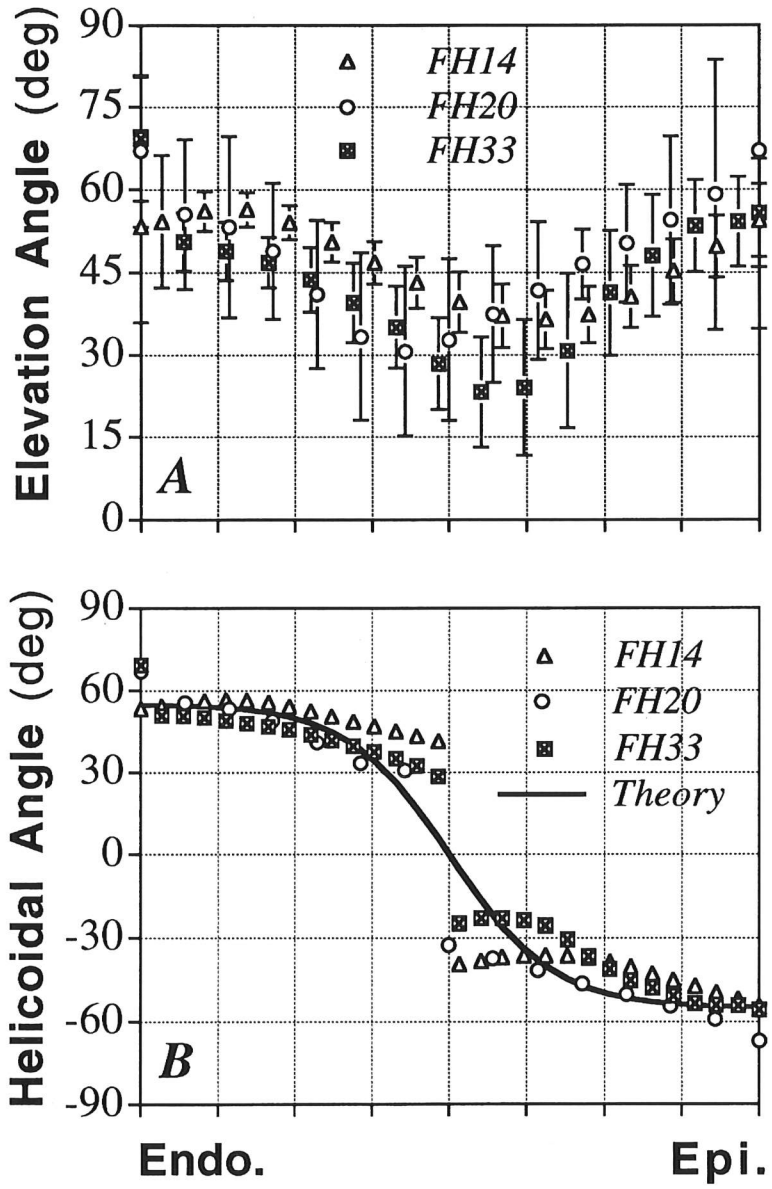

FIGURE 4 **A)** Mean radial distributions of the elevation fibre angle γ_{ele} measured in the lateral wall of the left ventricle from endocardium (endo.) to epicardium (epi.) for the fetal hearts of 14 weeks (FH14), 20 weeks (FH20), and 33 weeks (FH33) of gestational age. Unit of γ_{ele} is in degree. Note the similitude between the three curves. Bars represent the standard deviations. **B)** Mean radial distributions of the helicoidal fiber angle γ_{hel} in the lateral wall of the left ventricle from endocardium to epicardium for the fetal hearts of 14 weeks (FH14), 20 weeks (FH20), and 33 weeks (FH33) of gestational age. The Units of γ_{hel} are degrees (see text for definition of γ_{hel}). The plain line is the theoretical distribution used for the simulations.

angle decreases (negative angle) toward the apex giving the clockwise twist previously described (Figure 2). These results have also been observed by Streeter [5] on human adult hearts.

The fourth one refers to the comparison of the traversing of fibres from endocardium to epicardium between the FH14, FH20 and FH33. Figure 3 shows that the basal distributions of the transverse angle seems related to the gestational age of the FH.

2.3 Relationships between the Measurements and the Model Hypothesis

To keep the problem mathematically tractable, we have developed a model of LV mechanics using a simple geometric approximation such as a thick-walled cylinder. Cylindrical models are probably confined at best to describing the mechanics of the central portion (e.g. equatorial) of the human fetal LV.

The first assumption concerns the spatial distribution of the elevation angle. Based on the results in the literature [1,2,3,4,5] we assume that this angle changes in sign at midwall (Figure 4B). Our measurement method cannot distinguish positive γ_{ele} from negative γ_{ele} (see section 2.1). Nevertheless, observations made on longitudinal sections of hearts at the same stages confirmed this assumption. Therefore we define a new angle called the helicoidal angle (noted γ_{hel}) which is obtained as follows: $\gamma_{hel} = \gamma_{ele}$ from endocardium to midlayer, and $\gamma_{hel} = -\gamma_{ele}$ from midlayer to epicardium.

Our measurements of the direction field $\underset{\sim}{\tau}$ provide a basis for constructing an anisotropic continuum theory for myocardium. Although only $\underset{\sim}{\tau}$ itself is needed in the mathematical description, it is conceptually useful to determine the fibre paths by integrating the direction field in a cylindrical geometry:

$$\underset{\sim}{\tau} = \cos\gamma_{hel}(R, Z)\sin\gamma_{tra}(R, Z)\underset{\sim}{e_r} + \cos\gamma_{hel}(R, Z) \times \cos\gamma_{tra}(R, Z)\underset{\sim}{e_\theta} + \sin\gamma_{hel}(R, Z)\underset{\sim}{e_z} \quad (3)$$

where $(\underset{\sim}{e_r}, \underset{\sim}{e_\theta}, \underset{\sim}{e_z})$ is the cylindrical referential associated to the coordinates (R, θ, Z). We have computed the trajectory of the fibres for the three human FH, by assuming axial symmetry of the measured transverse angle in the lateral wall of the LV (Figures 3A, 3B and 3C) and by using a same distribution of helicoidal angle invariant from base to apex (Figure 4B, theoretical curve). Knowing that the transverse sections are cut perpendicular to the long axis of the LV and that in the central portion of the three LV the curvature is small, we can use the spatial distributions of the azimuth and helicoidal angles given in Figures 3 and 4B to estimate the fibre pathways. Moreover, we assume that the base-apex distribution of the transverse angle varies continuously between the measured basal, and apical distributions through the equatorial distribution (Figure 3) according to the law $tg(\gamma_{tra}) = h_r(R)h_z(Z)$. The function h_r gives the radial variation of the $tg(\gamma_{tra})$ between the endocardium and the epicardium, and the function h_z gives the axial variation of the $tg(\gamma_{tra})$ between the base and the apex. For our numerical simulations h_r is the tangent of the apical distribution of the transverse angle for the FH14 and FH20 (Figures 3A, 3B), and for the FH33 the function h_r is the tangent of the basal distribution of γ_{tra} (Figure 3C). The functions $h_z(-1 \leq h_z \leq 1)$ used to derive the pathways of the fibres in each FH are given in Figure 5.

As derived by Chadwick [9] from Streeter's measurements [5], in a longitudinal section through the wall, the projection of the computed direction field into a meridional plane (or RZ plane) defines a continuum of nested closed curves (Figures 6A, 6B and 6C). If these curves are then rotated about the axis of revolution of the LV, they define a system of nested toroidal surfaces on which all fibres are running in parallel. A fibre path lies on one of these toroids and winds around its surface in a helical manner. If we follow one fiber on a toroidal shell of revolution we can find the number of rotations (NR) done by this fibre on that shell before it returns to its initial position. The maximum number of rotations appears always on shells close to the *nodal* point and NR is almost the same for all toroidal shells of a single heart. The nodal point is defined as the position

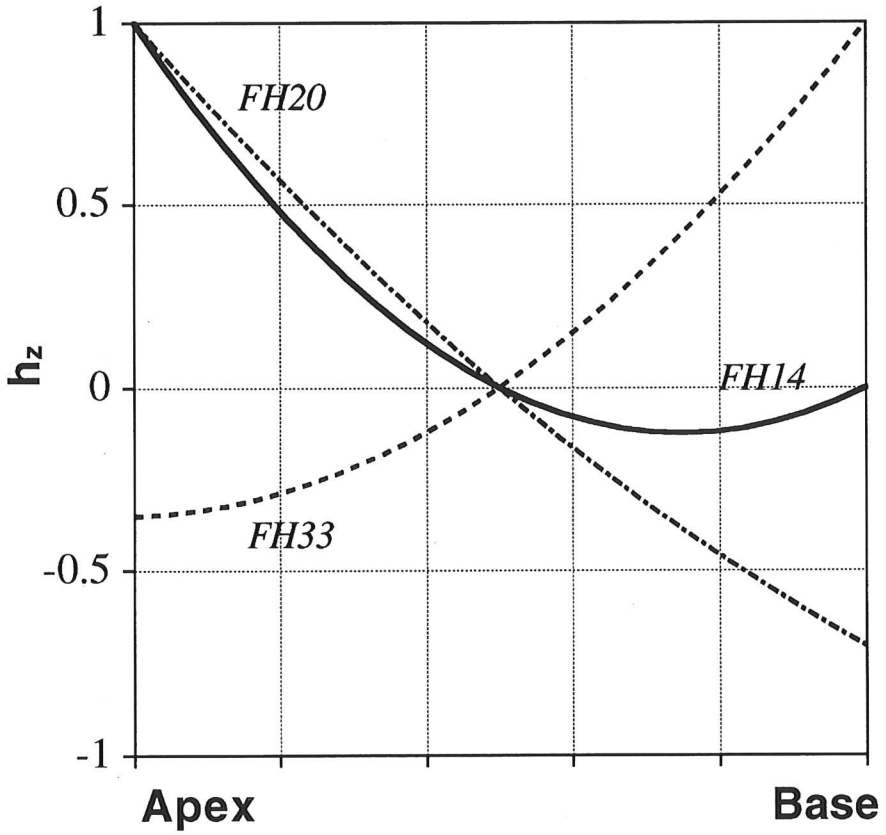

FIGURE 5 Normalized function $h_z(-1 \leq h_z \leq 1)$ describing the longitudinal variation of the $tg(\gamma_{tra})$ used to derive the pathways of the fibres in the fetal hearts of 14 weeks (FH14), 20 weeks (FH20), and 33 weeks (FH33) of gestational age (see text for details).

where the radius of the toroidal shell of revolution is zero which is equivalent to one circumferential fibre in the myocardium. This point is at the equator and approximately midwall. The calculation gives NR ≈ 2 for the FH14, NR ≈ 7 for the FH20, and NR ≈ 8 for the FH33. One must be careful when interpreting the later numbers (NR) because we are only considering the LV and we exclude the eventuality that fibres could escape the LV wall to pass in the RV wall. Moreover we neglect the complexity of the interventricular septum where fibres of the LV and RV intermingle.

Each individual myocardial cell located on the most apical or basal point of the toroidal shell has zero γ_{ele}. This is not observed in our measurements (Figure 4) because each voxel integrates about 2000 myocardial cells and because the alleged nested shells are not necessarily perfectly coaxial.

3. MECHANICS OF THE LEFT VENTRICLE

3.1 Continuum Description of the Myocardium and Equations of the Model

The myocardium is described as an incompressible fluid-muscle fibres-collagen continuum. To be consistent with our mathematical formulation we specify that the subscript '$\sim$' is used for a vector and the brackets '[]' are used for a matrix. The fluid-fibre-collagen stress tensor $[\sigma]$ used in this study can be viewed as a modified Peskin law [27] which takes care of the surrounding collagen matrix [11]:

$$[\sigma] = -P[I] + T[\underset{\sim}{\tau} \otimes \underset{\sim}{\tau}] + 2\mu[\varepsilon] \qquad (4)$$

where P stands for a term that results from the hydrostatic pressure due to the fluid and from the incompressibility of the solid medium [28]. Since P

has the same dimension as a pressure, we call it *tissue pressure*, it may be regarded as a Lagrangian multiplier. $[I]$ is the unit matrix, T is the tension in the fibre where the local fibre direction is given by the unit vector $\underset{\sim}{\tau}$ of components τ_i, μ is the effective shear modulus of the isotropic collagen matrix connecting the muscle fibres, and $[\varepsilon]$ is the strain tensor of components ε_{ij}.

The relationship between cardiac fibre tension T and fibre strain ε_f is approximated by a linear relationship [9], both in the passive state (characterized by the elastic modulus E) and in the maximally active state (characterized by the elastic modulus E^* and active tension at zero strain, T_0). During the cardiac cycle the fibre rheological behaviour is represented by a linear combination of these two states using the time-dependent activation function $\beta(t)$, $(0 \leq \beta \leq 1)$:

$$T = E_f(t)\varepsilon_f + \beta T_0 \text{ with } E_f(t) = (1-\beta)E + \beta E^* \tag{5a, b}$$

where ε_f represents the linearized fibre strain ($\varepsilon_f = \tau_i \varepsilon_{ij} \tau_j$). The end-diastolic state is represented by $\beta = 0$ and the end-systolic state, by $\beta = 1$.

Neglecting the effects of gravity, inertia and viscoelasticity of the medium, the basic problem is then to find single-valued displacement vector $\underset{\sim}{U}$ and tissue-pressure field P that satisfy the local equilibrium equation:

$$\nabla P = \mu \Delta \underset{\sim}{U} + \underset{\sim}{\tau}(T\nabla \cdot \underset{\sim}{\tau} + \underset{\sim}{\tau} \cdot \nabla T) + T[\nabla \underset{\sim}{\tau}]\underset{\sim}{\tau} \tag{6}$$

and the linearized condition of incompressibility

$$\nabla \cdot \underset{\sim}{U} = 0 \tag{7}$$

for a particular geometry and boundary conditions specified below. The symbols ∇ and Δ are respectively the vector *nabla* and the Laplacian operator.

3.2 LV Geometry and Fiber Direction Field

We work with a cylindrical referential $(\underset{\sim}{e_r}, \underset{\sim}{e_\theta}, \underset{\sim}{e_z})$ associated to the coordinates (R, θ, Z) to describe the boundaries of the axisymmetric LV geometry. This axisymmetric shape is a thick-walled finite cylinder where the base is located at $Z = 0$, the apex at $Z = -L$, the endocardium at $R = R_i$, and the epicardium at $R = R_e$. In terms of the scaled coordinates $r = R/R_i$ and $z = Z/R_i$, the lateral surfaces are given by $r_{\text{endo}} = 1$ and $r_{\text{epi}} = \alpha$ where $\alpha = R_e/R_i$.

In agreement with the fibre direction field shown previously (Equation 3) and by assuming for our perturbation theory that the transverse angle is small, the unit vector $\underset{\sim}{\tau}$ can be written as:

$$\underset{\sim}{\tau} = \lambda a(r, z)\underset{\sim}{e_r} + \cos\gamma_{\text{hel}}(r, z)\underset{\sim}{e_\theta} + \sin\gamma_{\text{hel}}(r, z)\underset{\sim}{e_z} \tag{8}$$

where λ is a small dimensionless parameter ($\lambda \ll 1$) controlling the amount of deviation. The first term of Equation (8) is needed to introduce the observed transverse fibre angle γ_{tra}. This latter angle is defined by $\gamma_{\text{tra}}(r, z) = \text{Arc } tg(\underset{\sim}{\tau}\cdot\underset{\sim}{e_r}/\underset{\sim}{\tau}\cdot\underset{\sim}{e_\theta}) = \text{Arc } tg(\lambda h(r, z))$ where for convenience we choose $a(r, z) = h(r, z)\cos\gamma_{\text{hel}}(r, z)$. So for our calculations, the function h(r,z) is directly related to the transverse fibre angle γ_{tra}.

A cylinder with regular helicoidal fibres running on cylindrical surfaces is described by a(r,z)=0, while the case of a cylinder with fibres running in a helical manner on toroidal shells of revolution is described by $a(r, z) \neq 0$ (Figure 6).

3.3 Boundary Conditions

We apply the conditions of continuity of stresses at the endocardium and epicardium which are given respectively by:

$$([\sigma]\cdot\underset{\sim}{e_r}) = -P_{lv}\underset{\sim}{e_r} \quad \text{on} \quad r = r_{\text{endo}} \tag{9a}$$

$$([\sigma]\cdot\underset{\sim}{e_r}) = \underset{\sim}{0} \quad \text{on} \quad r = r_{\text{epi}} \tag{9b}$$

where P_{lv} is the uniform LV cavity pressure.

The normal state of deformation of the structure includes torsion of the cylinder due to the rotation of the apex, which is free to rotate with respect to the assumed partially fixed base ($U_z = U_\theta = 0$ on $z = 0$) but radially free to move. Global static equilibrium requires that the net vertical force F and moment M acting on the apical surface of the

Therefore, all dependent variables $\varepsilon_{ij}, \varepsilon_f$, $\overline{T} = T/\mu$, and $\sigma_{ij} = \sigma_{ij}/\mu$ are expanded in the form, $\Phi = \Phi^{(0)} + \lambda\Phi^{(1)} + \cdots$, where Φ symbolizes each of the above quantities. The terms $\Phi^{(0)}$ are the fields for helicoidal fibres running on cylindrical surfaces with a uniform base to apex distribution of elevation angle in a cylindrical LV geometry, and the terms $\Phi^{(1)}$ are the corrections for a non-zero transverse fibre angle distribution.

Using these last results the expansion in term of λ of the unit fibre direction vector $\underset{\sim}{\tau}$ is:

$$\underset{\sim}{\tau} = \underset{\sim}{\tau}^{(0)} + \lambda\underset{\sim}{\tau}^{(1)} + \cdots \tag{11a}$$

$$\text{with } \underset{\sim}{\tau}^{(0)} = \cos\gamma^{(0)}_{\text{hel}(r)}\,\underset{\sim}{e_\theta} + \sin\gamma^{(0)}_{\text{hel}(r)}\,\underset{\sim}{e_z} \tag{11b}$$

$$\text{and } \underset{\sim}{\tau}^{(1)} = \cos\gamma^{(0)}_{\text{hel}(r)} h(r,z)\underset{\sim}{e_r} \tag{11c}$$

The problem is axisymmetric ($\partial/\partial\theta = 0$). The substitution of the Equations (10a–11c) into the Equations (6,7) and into the boundary conditions Equations (9a–d) and the regrouping of the first-order terms in λ gives two systems. The O(1) system together with its boundary conditions determine the equilibrium of the thick wall cylinder with uniform base to apex distribution of helicoidal fibre angle $\gamma^{(0)}_{\text{hel}(r)}$, and its solution has been given previously [11]. The O(λ) system determines corrections for fibres running on noncylindrical surfaces due to the introduction of the transverse fibre angle distribution, and is given by:

$$\nabla\overline{P}^{(1)} = \Delta\underset{\sim}{u}^{(1)} + \underset{\sim}{\xi}^{(1)} + \underset{\sim}{\chi}^{(1)} \tag{12a}$$

$$\nabla\cdot\underset{\sim}{u}^{(1)} = 0 \tag{12b}$$

with

$$\underset{\sim}{\xi}^{(1)} = (\overline{T}^{(0)}\nabla\cdot\underset{\sim}{\tau}^{(1)} + \underset{\sim}{\tau}^{(0)}\cdot\nabla\overline{T}^{(1)} + \underset{\sim}{\tau}^{(1)}\cdot\nabla\overline{T}^{(0)})\underset{\sim}{\tau}^{(0)} \tag{12c}$$

$$\underset{\sim}{\chi}^{(1)} = \overline{T}^{(0)}[\nabla\underset{\sim}{\tau}^{(0)}]\underset{\sim}{\tau}^{(1)} + (\overline{T}^{(0)}[\nabla\underset{\sim}{\tau}^{(1)}] + \overline{T}^{(1)}[\nabla\underset{\sim}{\tau}^{(0)}])\underset{\sim}{\tau}^{(0)} \tag{12d}$$

$$\overline{T}^{(0)} = \overline{E}_f\varepsilon_f^{(0)} + \beta\overline{T}_o \tag{12e}$$

$$\overline{T}^{(1)} = \overline{E}_f\varepsilon_f^{(1)} \tag{12f}$$

$$\text{and } \varepsilon_f^{(1)} = ([\varepsilon]^{(0)}\underset{\sim}{\tau}^{(1)} + [\varepsilon]^{(1)}\underset{\sim}{\tau}^{(0)})\cdot\underset{\sim}{\tau}^{(0)} + ([\varepsilon]^{(0)}\underset{\sim}{\tau}^{(0)})\cdot\underset{\sim}{\tau}^{(1)} \tag{12g}$$

In developing the O(λ), the lateral boundary conditions (Equations 9a,b) give:

$$\overline{\sigma}^{(1)}_{rz} = 0 \quad \text{on} \quad r = 1, \alpha \tag{13a, b}$$

$$\overline{\sigma}^{(1)}_{r\theta} = 0 \quad \text{on} \quad r = 1, \alpha \tag{13c, d}$$

$$\overline{\sigma}^{(1)}_{rr} = 0 \quad \text{on} \quad r = 1, \alpha \tag{13e, f}$$

and the conditions of apical equilibrium of forces and moments, Equations (9c,d), become respectively:

$$\overline{F}^{(1)} = \int_1^\alpha \overline{\sigma}^{(1)}_{zz} r\,\mathrm{d}r = 0 \quad \text{on } z = \ell \tag{13g}$$

$$\overline{M}^{(1)} = \int_1^\alpha \overline{\sigma}^{(1)}_{\theta z} r^2\,\mathrm{d}r = 0 \quad \text{on } z = \ell \tag{13h}$$

where $\overline{F}^{(j)} = F^{(j)}/(2\pi\mu R_i^2)$ and $\overline{M}^{(j)} = M^{(j)}/(2\pi\mu R_i^3)$ for $(j = 0, 1)$.

Note that the total equilibrium of the apical plate is described by:

$$\overline{F}^{(0)} + \lambda\overline{F}^{(1)} = 0 \tag{14a}$$

$$\overline{M}^{(0)} + \lambda\overline{M}^{(1)} = 0 \tag{14b}$$

and if $\overline{F}^{(1)} = \overline{M}^{(1)} = 0$ then the uniform system satisfies $\overline{F}^{(0)} = \overline{M}^{(0)} = 0$.

3.5 Solution of the O(λ) Perturbation System by Fourier Series

In spite of the linearity of the problem, the perturbed system cannot be treated separately. At a given time, the O(1) system associated to its boundary conditions is solved first. From this solution, the O(λ) system (Equations 12a–g) with associated boundary conditions (Equations 13a–h) can be solved and its solution is addressed in this work. The blockdiagram of the calculations is given in Figure 7.

In order to solve the O(λ) system, we express the known spatial distribution function h_z(z) by a

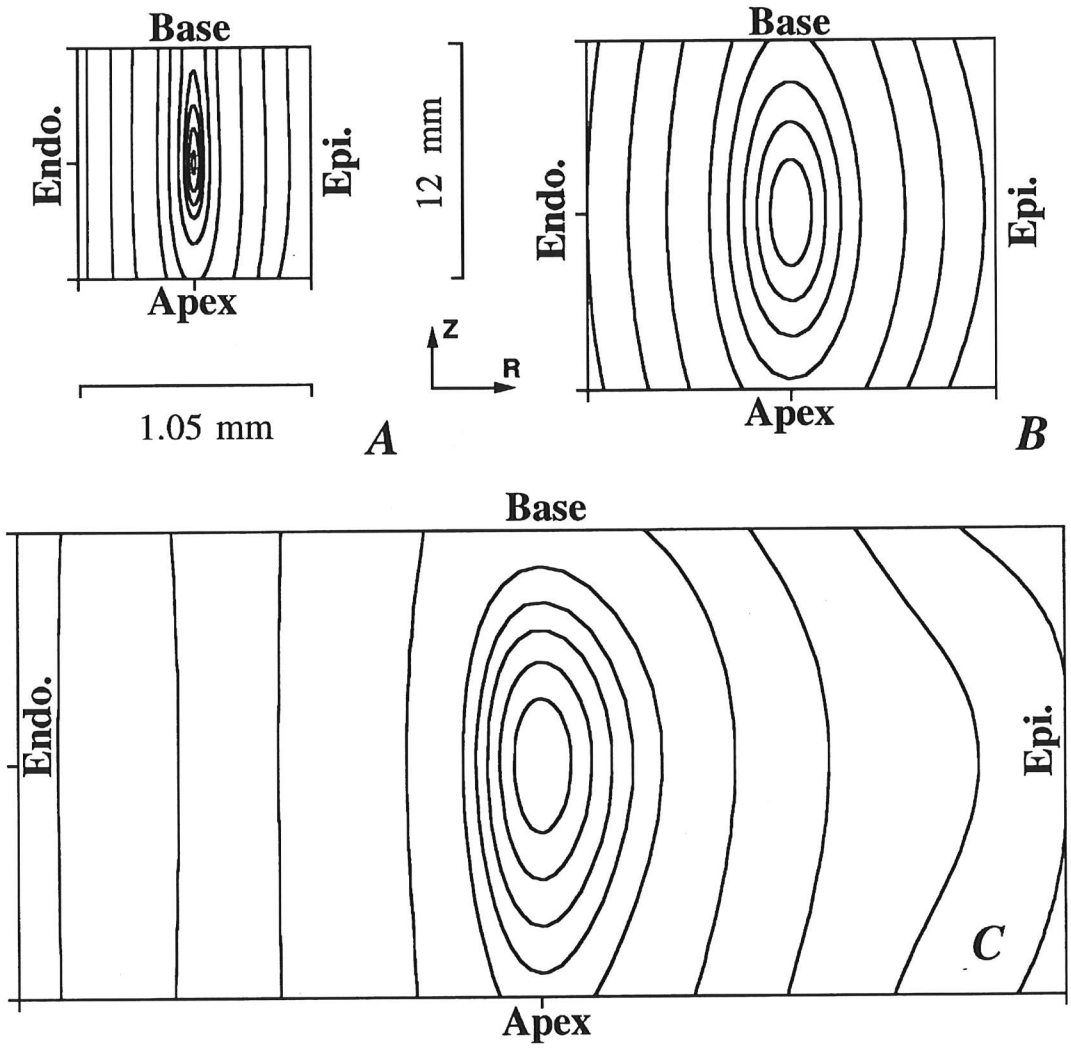

FIGURE 6 The projection of the computed fibre direction into a longitudinal section through the myocardium (RZ plane) gives a family of closed curves. These curves are rotated about the axis of revolution of the left ventricle and define a family of toroidal surfaces of revolution. The fibres are running on these shells in a helical manner. The R and Z scales are different. In order to compare the size of the hearts during fetal development, we kept the same R and Z scales for the fetal hearts of A) 14 weeks (FH14), B) 20 weeks (FH20), and C) 33 weeks (FH33) of gestational age. Endo.: endocardium, Epi.: epicardium.

cylinder are zero:

$$\frac{F}{2\pi R_i^2} = \int_{r_{\text{endo}}}^{r_{\text{epi}}} \sigma_{zz} r \mathrm{d}r - \int_0^{r_{\text{endo}}} P_{lv} r \mathrm{d}r = 0 \quad \text{on} \quad z = \ell \tag{9c}$$

$$\frac{M}{2\pi R_i^3} = \int_{r_{\text{endo}}}^{r_{\text{epi}}} \sigma_{\theta z} r^2 \mathrm{d}r = 0 \quad \text{on} \quad z = \ell \tag{9d}$$

where $\ell = -L/R_i$.

3.4 Asymptotic Expansion Procedure

The plan is to work with the scaled rheological parameters $\overline{E}_f = E_f/\mu; \overline{T}_o = T_o/\mu$, the scaled pressures $\overline{P} = P/\mu; \overline{P}_{lv} = P_{lv}/\mu$, and to expand the unknown components of the scaled displacement field $u_i = U_i/R_i$ and tissue pressure $\overline{P}$ in the form [29]:

$$u_i = u_i^{(0)} + \lambda u_i^{(1)} + \cdots \tag{10a}$$

$$\overline{P} = \overline{P}^{(0)} + \lambda \overline{P}^{(1)} + \cdots . \tag{10b}$$

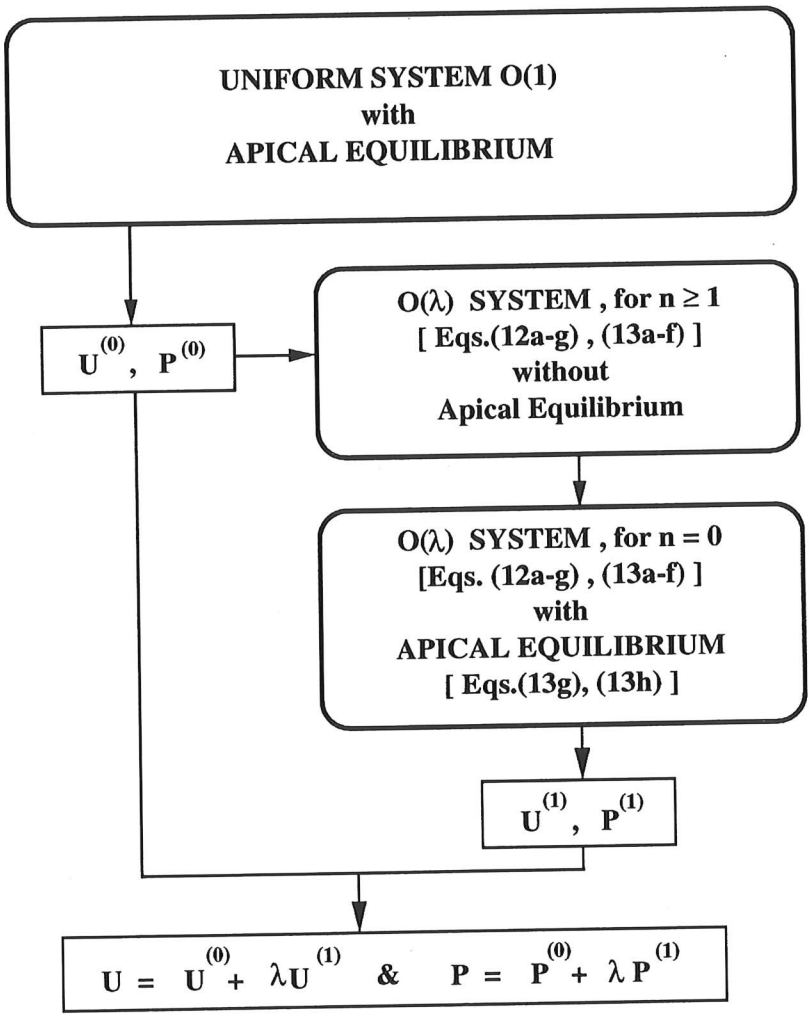

FIGURE 7 Algorithm for solving the coupled systems (see text for details).

Fourier representation:

$$h_z(z) = \sum_{n=1}^{\infty} h_n \sin(k_n z) \quad \text{with } k_n = \frac{n\pi}{\ell} \tag{15}$$

where $h(r, z) = h_z(z)h_r(r)$.

Likewise, we express the normalized displacement field $u_i^{(1)}$ and the scaled tissue pressure $\overline{P}^{(1)}$ in the form

$$u_r^{(1)}(r, z, t) = u_{r(n=0)}^{(1)} + \sum_{n=1}^{\infty} X_n(r, t)\cos(k_n z) \tag{16a}$$

$$u_\theta^{(1)}(r, z, t) = u_{\theta(n=0)}^{(1)} + \sum_{n=1}^{\infty} Y_n(r, t)\sin(k_n z) \tag{16b}$$

$$u_z^{(1)}(r, z, t) = u_{z(n=0)}^{(1)} + \sum_{n=1}^{\infty} Z_n(r, t)\sin(k_n z) \tag{16c}$$

$$\overline{P}^{(1)}(r, z, t) = \overline{P}_{(n=0)}^{(1)} + \sum_{n=1}^{\infty} P_n(r, t)\cos(k_n z) \tag{16d}$$

(1) Solution for $n \geq 1$

For $n \geq 1$, this form of the displacement field satisfies the kinematic conditions of zero axial and circumferential displacements at the base, $z = 0$. Substitution of Equation (15) and Equations (16a–d) into the equilibrium and incompressibility equations (12a–g), and into the lateral boundary conditions Equations (13a,f), using the independence of $\cos(k_n z)$

and $\sin(k_n z)$, results, for each spatial frequency ($n = 1, \infty$), in a system of six coupled first-order ordinary differential equations for $(X_n, Y_n, Z_n, P_n, Y'_n, Z'_n)$ together with three boundary conditions each on $r = 1, \alpha$.

(2) *Solution for* $n = 0$

When $n = 0$, the solution is similar to the solution of the uniform system O(1) [11] and corrects the axial equilibrium of the apical plate which was not satisfied by the previous solution of the perturbed system for $n \geq 1$.

4. NUMERICAL RESULTS AND DISCUSSION

The O(λ) system with the two-point boundary conditions was solved numerically on a Silicon Graphics Indy 5000SC/180 Mhz using the International Mathematical Statistical Libraries (IMSL) routine BVPMS based on a multiple shooting method. The simulations are done with twenty five harmonics ($n = 25$) and with a perturbation parameter $\lambda = 10\%$. In order to analyse the effect of the transverse angle on the mechanics of the fetal LV, we compare the results obtained with transverse angle to the first-order solution which is also the solution at the equator. The following estimates correspond to numerical absolute errors which are made in our calculations: $10^{-7}R_i$ for the displacements, $10^{-7}\mu$ for the stresses, 10^{-7} ml for the LV volume, $10^{-4}\%$ for the strains and $2 \times 10^{-4}\%$ for the ejection fraction (EF).

A list of the chosen parameter values for the three FH is given in Table I. Values of LV end-diastolic volumes (V_{ed}) and EF for the human FH of 14, 20 and 33 weeks of gestational age are readily found in the literature [30,31,32]. From the range of values given by [30,31] a low value of the ejection fraction is chosen to satisfy the linear theory of elasticity (EF = 0.4). The initial configurations (L, R_i and $\alpha = R_e/R_i$) are derived from the three analyzed FH. We were unable to find values for the end-diastolic and end-systolic pressures (noted respectively P_{ed} and P_{es}) in human species in the literature and therefore regard them as a free parameters. We were also unable to find values for the rheological parameters of the human FH. For the passive state we use the experimental results of Demer and Yin [33] obtained on passive myocardium to derive the material constants $E = 20$ kPa and $\mu = 2$ kPa [11]. For the active state we use the experimental results of Pinto [34] done on active papillary muscle to determine the material constants $E^* = 200$ kPa and $T_o = 31$ kPa. Moreover, we assume that the mechanical properties of the heart do not change during development. Obviously, this assumption may not be valid, but few data are available to determine how these properties change. Friedman [35] found that developed tension is less in fetal lambs than in adult sheep. This finding supports the idea of decreased contractility in the fetus. Because the FH was composed of only 30% myofibrils as opposed to the adult heart with 60%, Friedman suggested that the contractility of individual sarcomeres was similar in fetal and adult hearts, but there was simply more contractile material in

TABLE I Assumed values for the parameters of the model

	Fetal Heart		
	14 weeks	20 weeks	33 weeks
V_{ed} (m^3)	0.2×10^{-6}	0.4×10^{-6}	2.7×10^{-6}
EF	0.4	0.4	0.4
R_i (m)	0.213×10^{-2}	0.274×10^{-2}	0.532×10^{-2}
L (m)	1.200×10^{-2}	1.480×10^{-2}	2.475×10^{-2}
$\alpha = R_e/R_i$	1.5	1.7	1.9
E (kPa)	20	20	20
μ (kPa)	2	2	2
E^* (kPa)	200	200	200
T_o (kPa)	31	31	31

adult hearts. Based on the Friedman's conclusions, we kept the same active rheological parameters E^* and T_o for the three FH. Concerning the passive properties of the myocardium it is known that the density of collagen in the myocardium increases slightly with the gestational age. In fact the main change occurs during postnatal heart development [36], we can assume that the passive rheological parameters E and μ stay the same during fetal life.

Figure 8 shows computed pressure-volume loops of the three fetal LV obtained during one cardiac cycle by assuming isovolumic contraction and relaxation phases, isobaric ejection and filling phases. The calculated end-systolic LV pressures P_{es} (25 mmHg, 35 mmHg and 50 mmHg respectively for the FH14, FH20 and FH33) are in the order of the measured mean arterial blood pressure during fetal sheep period [37]. For the end-diastolic LV pressures P_{ed} our calculations (2.5 mmHg, 2.5 mmHg and 4.2 mmHg respectively for the FH14, FH20 and FH33) are in agreement with the passive pressure-volume curves obtained on fetal sheep ventricles [38].

The transmural distributions of end-systolic fibre strain are very similar for the three FH (Figure 9). We found no significant deviations from the first-order solution when we computed the fibre strain at several longitudinal locations. The main end-systolic fibre shortening occurs on the subendocardial and subepicardial layers. In the central layers where the fibres are almost circumferential, the end-systolic fibre strain is small. As already shown by Bovendeerd *et al.* [39], these results are very sensitive to the helicoidal angle distribution. The transmural distribution of fibre tension is not plotted, but could be easily derived from Equation (5) knowing the distribution of fibre strain.

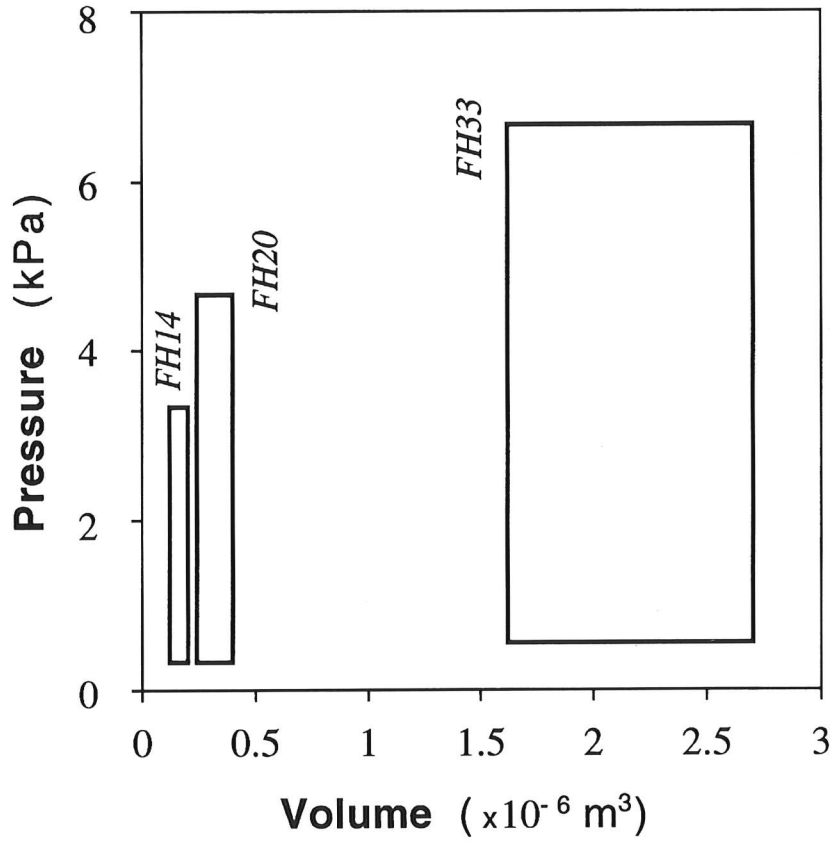

FIGURE 8 Computed left ventricular pressure-volume relations during one cardiac cycle for the fetal hearts of 14 weeks (FH14), 20 weeks (FH20), and 33 weeks (FH33) of gestational age (1 kPa $\approx$ 7.5 mmHg).

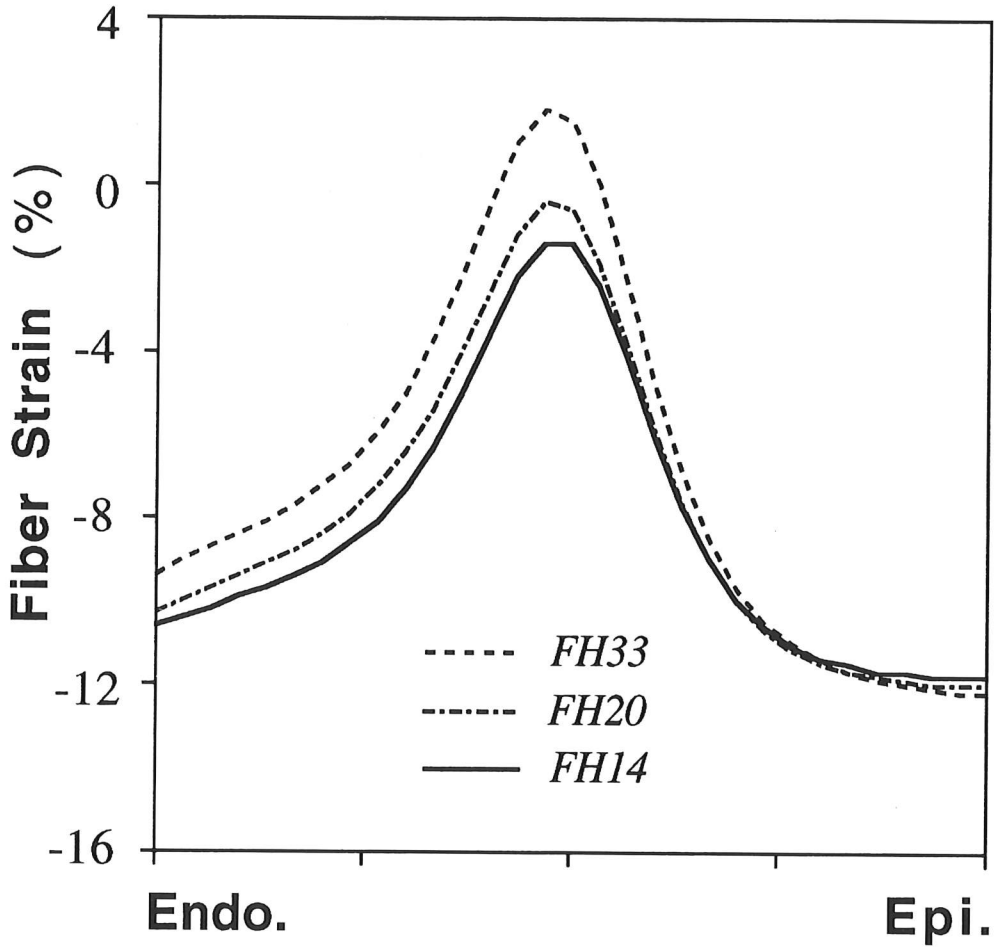

FIGURE 9 Computed uniform fibre strain distribution $\varepsilon_f^{(0)}$ from endocardium (endo.) to epicardium (epi.) at end-systole for fetal hearts of 14 weeks (FH14), 20 weeks (FH20), and 33 weeks (FH33) of gestational age. The strains are computed relatively to the passive unloaded configuration.

Ventricular wall thickening is an important mechanism for systolic ejection [40]. The introduction of a non-zero transverse fibre angle affects the radial strain and therefore the LV wall thickening. The transmural end-systolic distribution of radial strain for the FH33 is plotted in Figure 10 for several longitudinal locations at the apex ($z = \ell$), between apex and equator ($z = 3\ell/4$, curve *AE*), equator ($z = \ell/2$), between equator and base ($z = \ell/4$, curve *BE*) and base ($z = 0$). For the longitudinal locations near the equator (Figure 10, curves *AE* and *BE*) the myocardium becomes thicker than on the apical or basal sections, and the largest radial strains are on the endocardial layer. These observations on radial strain are also true for the other two FH. From our calculations it appears that the non-zero uniform normal stresses σ_{rr}, $\sigma_{\theta\theta}$, σ_{zz} and shear stress in the θz plane ($\sigma_{\theta z}$) are not affected by γ_{tra}. Nevertheless the introduction of γ_{tra} gives two new shear strains and stresses in the rz and $r\theta$ planes. As observed and measured by Young *et al.* [41] during systole, using magnetic resonance imaging on normal adult human hearts, the longitudinal variation of the $\varepsilon_{r\theta}$ shear strain changes sign from base to apex. For the calculations done on FH, this shear strain exists in the central layer (Figure 11) precisely at the point where the fibres, running in helical manner on a toroidal shell of revolution, go from endocardial

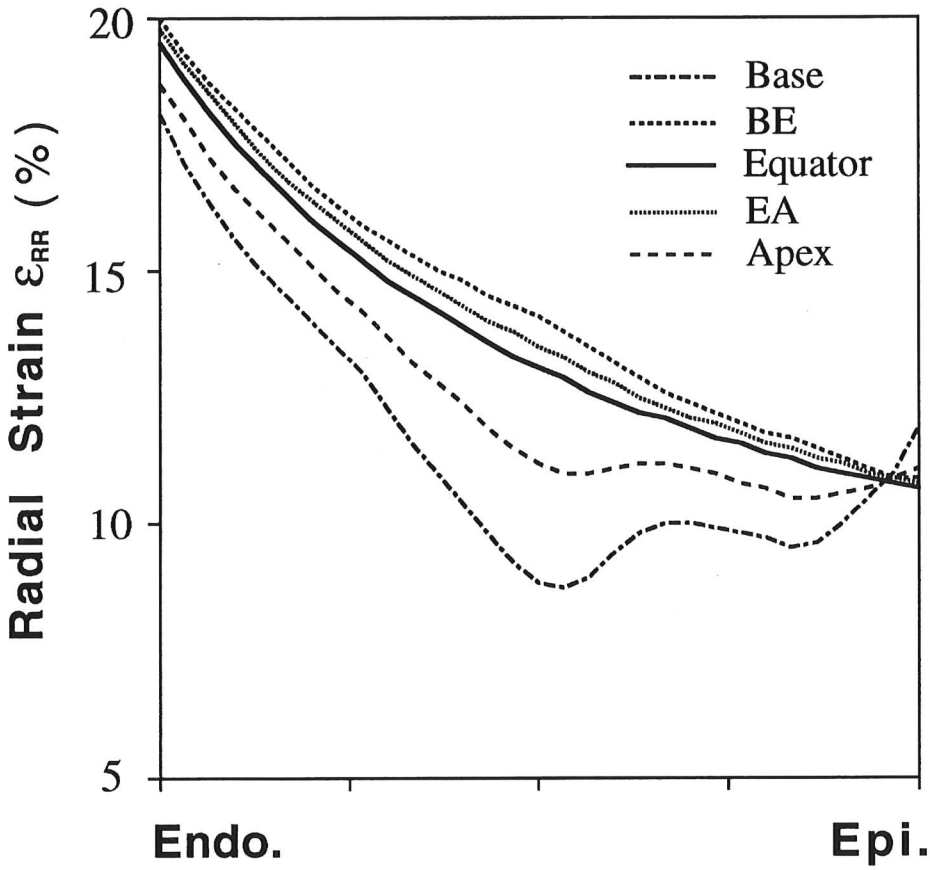

FIGURE 10 Computed radial strain distribution ε_{rr} from endocardium (endo.) to epicardium (epi.) at end-systole for fetal hearts of 33 weeks (FH33), at different longitudinal locations : apex ($z = \ell$), between apex and equator ($z = 3\ell/4$, curve *AE*), equator ($z = \ell/2$, equal to first-order solution), between equator and base ($z = \ell/4$, curve *BE*) and base ($z = 0$). The strains are computed relatively to the passive unloaded configuration.

layers to epicardial layers (Figure 6). The change of sign of $\varepsilon_{r\theta}$ from base to apex is related to the orientation of the projected fibre on the $r\theta$ section plane (Figure 2C) and therefore depends on the spatial transverse angle distribution. The amplitude of this shear strain is very sensitive to the amount of collagen in the myocardium and decreases if the shear modulus μ increases. The corresponding shear stress $\sigma_{r\theta}$ is small (less than 1 kPa) and if we compare the shapes of the spatial distributions of $\sigma_{r\theta}$ obtained from our model (Figure 12) with the radial distributions of the measured transverse angle (Figure 3), we find a high correlation.

Few mathematical models on the mechanics of the LV actually consider the transverse angle. Van Campen *et al.*, [21] used a finite element analysis model with a more realistic geometry to describe the mechanics of the beating adult LV and found that the ejection fraction (EF) and the magnitude of the rotation of the wall around the long axis are sensitive to the transverse fibre angle distribution γ_{tra}. Compared to the first-order solution, our results give for the three FH a decrease of the EF and the ejected volume near 1% when we take care of the measured transverse angle distribution. Moreover, to analyse the effect of the perturbation on the twist of the left ventricle, we compute at several longitudinal locations the mean torsion of a transverse section defined as:

$$\Theta(z) = \frac{1}{\alpha - 1} \int_1^{\alpha} \frac{u_\theta(r, z)}{r} \mathrm{d}r \qquad (17)$$

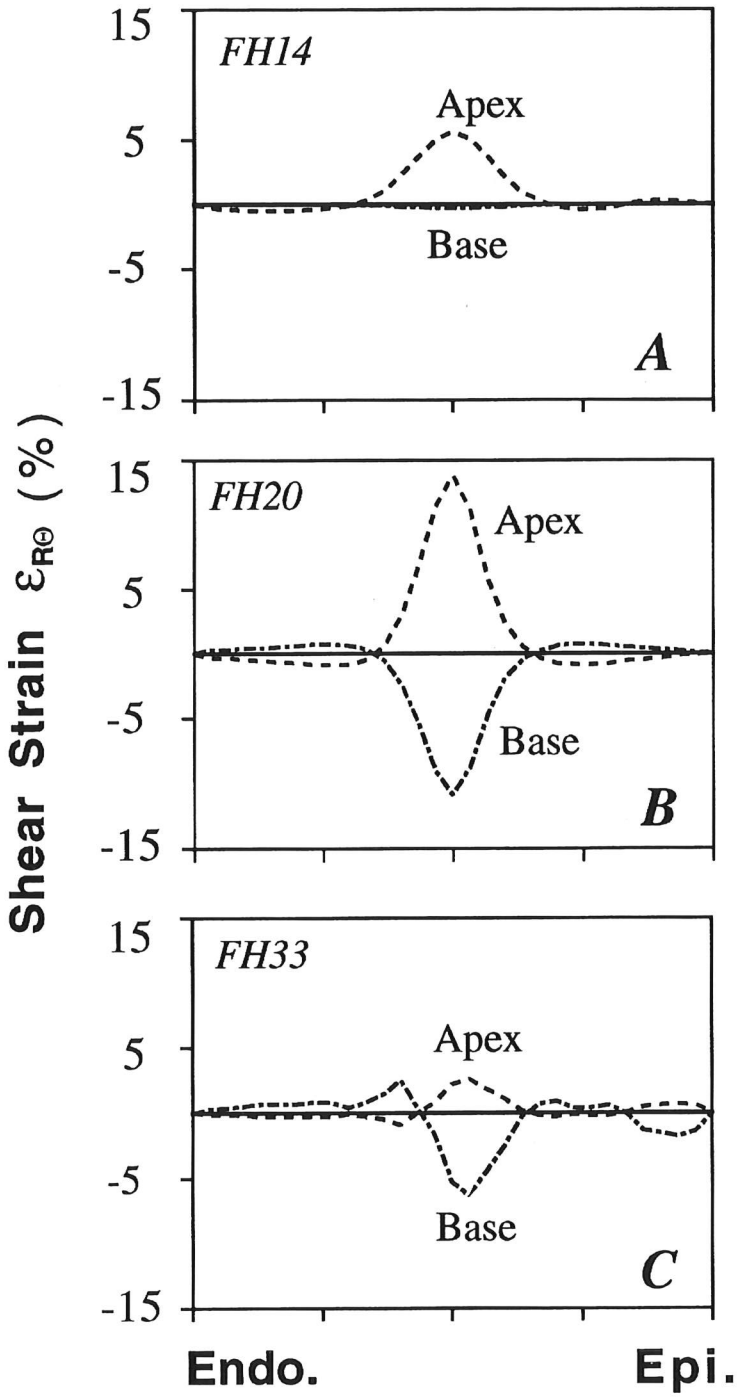

FIGURE 11 Computed spatial distributions of the shear strain $\varepsilon_{r\theta}$ in the lateral wall of the left ventricle at end-systole for the fetal hearts of A) 14 weeks (FH14), B) 20 weeks (FH20), and C) 33 weeks (FH33) of gestational age. One must note the main magnitude of the shear strain in the central layer and the opposition of sign of $\varepsilon_{r\theta}$ between base and apex, while it remains equal to zero at the equator (plain line). Endo.: endocardium, Epi.: epicardium. The strains are computed relatively to the passive unloaded configuration.

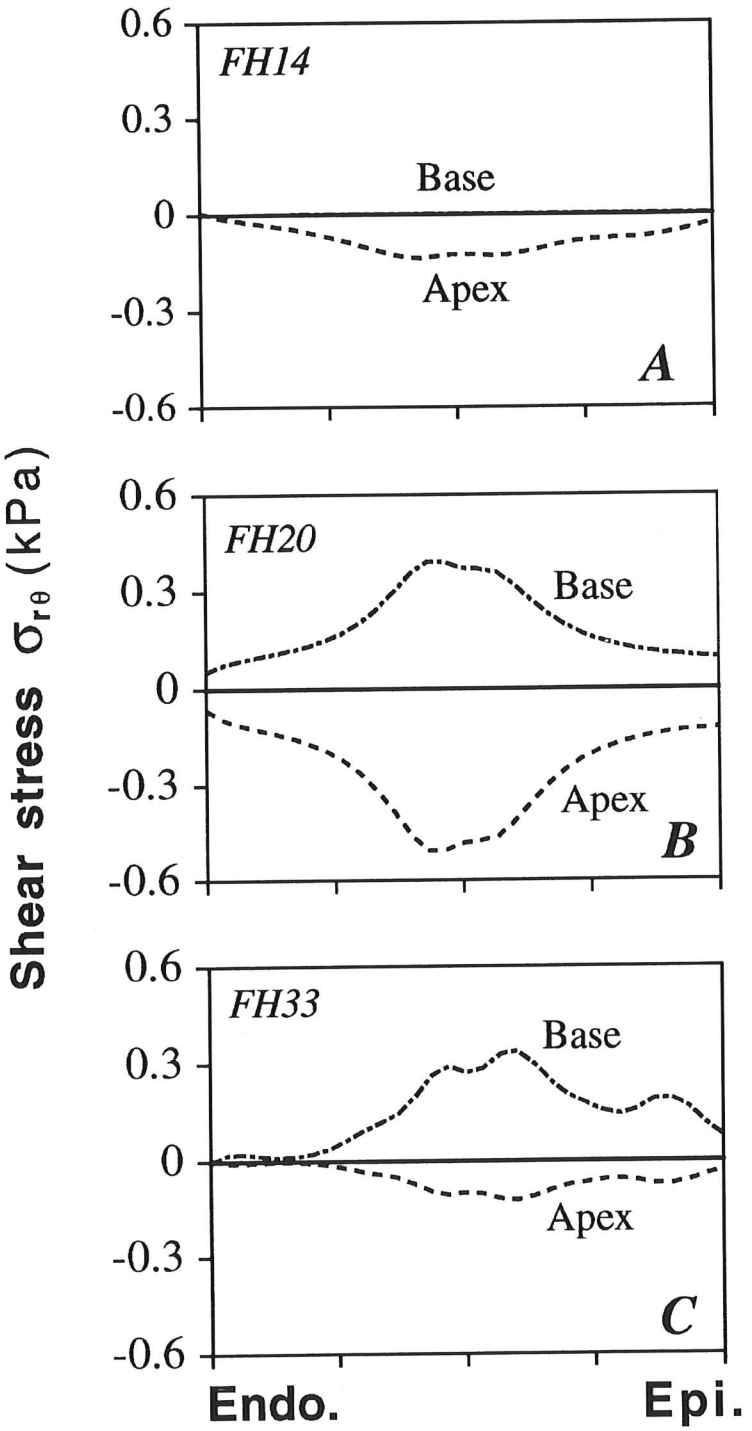

FIGURE 12 Computed spatial distributions of the shear stress $\sigma_{r\theta}$ in the lateral wall of the left ventricle at end-systole for the fetal hearts of A) 14 weeks (FH14), B) 20 weeks (FH20), and C) 33 weeks (FH33) of gestational age. One must note the similitude of the spatial distributions of shear stress and transverse angle given in Figure 3. $\sigma_{r\theta}$ remains equal to zero at the equator (plain line). Endo.: endocardium, Epi.: epicardium.

TABLE II Computed mean torsion with and without the transverse angle (respectively noted Θ and $\Theta^{(0)}$) at four longitudinal locations and at end-systole for the three fetal hearts. The variation of the relative change of mean torsion $\Theta^* = (\Theta - \Theta^{(0)})/\Theta^{(0)}$ of the left ventricle with reference to the uniform cylindrical solution at different axial levels is also given. The torsions Θ and $\Theta^{(0)}$ are computed relatively to the passive unloaded configuration

Fetal Heart	Midway from base to equator $z = \ell/4$	Equator $z = \ell/2$	Midway from equator to apex $z = 3\ell/4$	Apex $z = \ell$
14 weeks				
$\Theta^{(0)}$ *(deg)*	−2.83	−5.25	−8.48	−10.09
Θ *(deg)*	−3.10	−5.80	−9.44	−11.17
Θ^*	9.6%	10.5%	11.3%	10.6%
20 weeks				
$\Theta^{(0)}$ *(deg)*	−3.22	−5.97	−9.65	−11.49
Θ *(deg)*	−3.28	−6.58	−10.99	−12.82
Θ^*	1.9%	10.2%	13.9%	11.6%
33 weeks				
$\Theta^{(0)}$ *(deg)*	−3.03	−5.63	−9.10	−10.84
Θ *(deg)*	−3.10	−6.16	−10.13	−11.96
Θ^*	2.2%	9.2%	11.3%	10.4%

Table II gives the LV mean torsion with and without the transverse angle (torsions noted respectively Θ and $\Theta^{(0)}$) at four longitudinal locations and at end-systole for the three FH. The relative change of mean torsion of a transverse section $\Theta^* = (\Theta - \Theta^{(0)})/\Theta^{(0)}$ is also given in Table II. The largest effect on Θ^* comes from the introduction of a non-zero transverse fibre angle γ_{tra} and is localized at midway from equator to apex. Such spatial distributions of γ_{tra} (Figure 3) seem to increase the amplitude of the mean torsion ($\Theta^* > 0$).

Yang *et al.* [15] have measured the epicardial longitudinal, circumferential and shear strains (respectively ε_{zz}, $\varepsilon_{\theta\theta}$ and $\varepsilon_{z\theta}$) relative to end-diastole during cardiac cycle for a stage 21 chick embryo heart. Table III gives values of our numerical results computed from the first-order solution at the endocardium, midlayer and epicardium and the previous measured strains [15]. The agreement with the experimental data is quite good except for the circumferential strain. We have to be careful while comparing such results because embryonic development and fetal development are very different and we believe that at the beginning of the fetal period the organisation of the fibres and the geometry of the heart are already well defined and quite stable in regard to the embryonic period where the heart grows rapidly as it transforms from a muscle-wrapped tube into a septated four-chambered pump.

One of the limitations of our model is essentially due to the use of the perturbation theory where the transverse angle is so small that we must analyse only the tendency of our results relatively to the first-order solutions.

Since in this study we focus primarily on LV mechanics during systole when we consider toroidal shells of revolution in the myocardium, we have neglected the residual stresses and strains. The residual strains are important at stage 16 of the chick embryo and decrease between stages 16 and 18 corresponding to the onset of trabeculation, which is the greatest change in form during stages 16 to 24 [42]. The lower opening angles measured in an embryonic chick ventricle at stage 24 [42] were in the order of magnitude of those measured by Rodriguez *et al.* [43] in the mature rat LV ($45 \pm 15°$). The results of Rodriguez *et al.* show a uniform sarcomere length (SL) distribution across

TABLE III Values of first-order solution computed strains at end-systole relative to end-diastole for the FH of 33 weeks. This table gives also the values of the measured (15) longitudinal ε_{zz}, circumferential $\varepsilon_{\theta\theta}$ and shear $\varepsilon_{z\theta}$ strains at end-systole relative to end-diastole and at several longitudinal locations from endocardium to epicardium (see text for discussion)

Fetal Heart of 33 weeks	Calculated endocardium strains	Calculated central layer strains	Calculated epicardium strains	Measured epicardium strains (15)
$\varepsilon_{\theta\theta}$ (%)	−14.69	−3.93	0.53	≈ -10
ε_{zz} (%)	−14.16	−14.16	−14.16	≈ -12
$\varepsilon_{z\theta}$ (%)	2.15	3.11	4.08	≈ 3

the wall with a transmural average of 1.84 μm for the stress-free tissue (or zero-stress state). The same work shows that for the unloaded physiological stage the SL distribution decreases linearly from 1.90 μm at epicardium to 1.78 μm at endocardium. This last decrease corresponds to a residual strain going from 3% at epicardium to −3% at endocardium if we use a SL of 1.84 μm at the stress-free state. If we assume that such results are also true for human FH then the radial distributions of the fibre strain given in Figure 9 change slightly and the tendency stays the same.

In the adult circulation, the right ventricle, the lungs, the left heart and the systemic circulation are arranged in series. Blood flow through each of these elements is identical, and equals the cardiac output. In the fetal circulation, the left and right ventricle each pump blood into the arterial circulation in parallel. Working in parallel, the right ventricle (RV) ejects between 50% and 66% of the combined ventricular output, and the LV between 50% and 34%. Calculation of ventricular stroke volumes using a representative FH rate of 150 beats/min yields values of 2 ml per kg of body weight for the RV and 1 ml per kg of body weight for the LV. These may be compared to values of 1 ml/kg for each of the adult ventricles working in series [44]. Thus an elevated heart rate together with an elevated stroke volume (of the RV) explains the impressive pumping performance of the FH in comparison with the adult heart. In the FH the LV and RV eject blood into the arterial circuit, but distribution of the two ventricular outputs in the fetal body differs. Most blood ejected by the LV perfuses the upper body, whereas the lower body and placenta are largely perfused by the RV [45]. These last comments suggest that during the fetal period the analysis of the LV functions must be coupled to the analysis of the RV functions. Future work should address this point.

We presented a model to describe the performance of the human fetal LV. This model is based on direct use of anatomical data measured in 3 human FH at distinct gestational age. To keep the problem mathematically tractable, we used the simple axisymmetric geometry of the thick walled cylinder. The results of this study suggest the following conclusions.

The introduction of a non-zero transverse fibre angle into a model based classically on the variation of helicoidal angle:

1. gives a complex nested set of toroidal surfaces of revolution on which fibres are running in a helical manner.
2. has only a slight effect on systolic fibre strain distribution.
3. affects the LV wall thickening by increasing the end-systolic wall thickness in the nearly equatorial region.
4. increases the torsion of the LV, knowing that this torsion is also very sensitive to the helicoidal angle.
5. creates at end-systole midwall shear strains in the transverse plane. These shear strains are maximal at the most apical or basal point of the toroidal shells.

As a final remark, we again emphasize that the paucity of experimental data for the developing human FH forced us to make a number of assumptions that cannot be validated at present. One of the major limitations of our model is due to the use of a linear analysis. The linear model described in this paper cannot capture adequately many of the important effects due to the nonlinear nature of the myocardium. Nevertheless our model provides a starting point to study the mechanics of the fetal LV and shows the necessity to take care of the complex geometry of the shells on which fibres are running. These conclusions await further data on microstructure and material properties of the human fetal heart during development.

Acknowledgements

The authors are very grateful to Gabrielle Michalowicz and Laurence Grossi for excellent technical help, and to the referees for their useful comments. This work was supported by Groupe d'Etude de Langue Françcaise sur la Mort Subite du Nourrisson (GELFMSN), 1996.

References

[1] Torrent-Guasp, F. *The Cardiac Muscle*, (Fundación Juan March, Madrid, 1973).

[2] Greenbaum, R. A., Ho, S. Y., Gibson, D. G., Becker, A. E. and Anderson, R. H. (1981). Left ventricular fibre architecture in man, *British Heart Journal*, **45**, 248–263.

[3] Nielsen, P. M. F., LeGrice, I. J., Smaill, B. H. and Hunter, P. J. (1991). Mathematical model of geometry and fibrous structure of the heart, *American Journal of Physiology*, **260**, H1365–H1378.

[4] Hort, W. (1960). Makroskopische und mikrometrische untersuchungen am myokard verschieden stark gefüllter linker kammern, *Virchows Arch. Pathol. Anat.*, **33**, 523–564.

[5] Streeter, D. D. (1979). Gross morphology and fiber geometry of the heart. In *Handbook of Physiology* (eds. R. M. Berne, N. Sperelakis and S. R. Geiger), Am. Physiol. Soc., Bethesda, MD, **1**(2), 61–112.

[6] Jouk, P. S., Usson, Y., Michalowicz, G. and Parazza, F. (1995). Mapping of the orientation of myocardial cells by means of polarized light and confocal scanning laser microscopy, *Microscopy Research and Technique*, **30**, 480–490.

[7] Arts, T., Reneman, R. S. and Veenstra, P. C. (1979). A model of the mechanics of the left ventricle, *Annals of Biomedical Engineering*, **7**, 299–318.

[8] Feit, T. S. (1979). Diastolic pressure-volume relation and distribution of pressure and fiber extension across the wall of a model left ventricle, *Biophysical Journal*, **28**, 143–166.

[9] Chadwick, R. S. (1982). Mechanics of the left ventricle, *Biophyscal Journal*, **39**, 279–288.

[10] Tözeren, A. (1983). Static analysis of the left ventricle, Journal of Biomechanical Engineering, **105**, 35–46.

[11] Ohayon, J. and Chadwick, R. S. (1988). Effects of collagen microstructure on the mechanics of the left ventricle, *Biophysical Journal*, **54**, 1077–1088.

[12] Humphrey, J. D. and Yin, F. C. P. (1989). Constitutive relations and finite deformations of passive cardiac tissue II: Stress analysis in the left ventricle, *Circulation Research*, **65**, 805–817.

[13] Taber, L. A. (1991). On a nonlinear theory for muscle shells: Part II- Application to the beating left ventricle, *Journal of Biomechanical Engineering*, **113**, 63–71.

[14] Guccione, J. M., Waldman, L. K. and McCulloch, A. D. (1993). Mechanics of active contraction in cardiac muscle: Part II- Cylindrical models of the systolic left ventricle, *Journal of Biomechanical Engineering*, **115**, 82–90.

[15] Yang, M., Taber, L. A. and Clark, E. B. (1994). A nonlinear poroelastic model for the trabecular embryonic heart, *Journal of Biomechanical Engineering*, **116**, 213–223.

[16] Ohayon, J., Chadwick, R. S. and Herbin, R. (1995). Non-uniform cavity pressure and ventricular mechanics, *Mechanical Research Communications*, **22**, 205–219.

[17] Chadwick, R. S., Ohayon, J. and Lewkowicz, M. (1989). Wall thickness and midwall radius variations in ventricular mechanics, *Proceeding National Academic of Science, USA*, **86**, 2996–2999.

[18] Zidi, M., Boulos, M. and Oddou, C. (1989). Application of the finite element approximation to the cardiac mechanics, *5th International Symposium on Numerical Methods In Engineering*, **1**, 509–514.

[19] Crolet, J. M., Chahboune, B. and Akesbi, S. (1992). Presentation of mixed problem fluid-structure, *Proceeding 4th International Conference of Fluid Mechanics*, **5**, 1–6.

[20] McCulloch, A. D., Waldman, L. K., Rogers, J. M. and Guccione, J. M. (1992). Large-scale finite element analysis of the beating heart, *Critical Reviews in Biomedical Engineering*, **205**, 427–449.

[21] Van Campen D. H., Huyghe, J. M., Bovendeerd, P. H. M., and Arts, T. (1994). Biomechanics of the heart muscle, *European Journal of Mechanics, A/Solids*, **13**, 19–41.

[22] Costa, K. D., Hunter, P. J., Rogers, J. M., Guccione, J. M., Waldman, L. K. and McCulloch, A. D. (1996). A three-dimensional finite element method for large elastic deformations of ventricular myocardium: I-Cylindrical and spherical polar coordinates, *Journal of Biomechanical Engineering*, **118**, 452–463.

[23] Costa, K. D., Hunter, P. J., Wayne, J. S., Waldman, L. K., Guccione, J. M. and McCulloch, A. D. (1996). A three-dimensional finite element method for large elastic deformations of ventricular myocardium: II- Prolate spheroidal coordinates, *Journal of Biomechanical Engineering*, **118**, 464–472.

[24] Born, M. and Wolf, E. *Principles of Optics* (Pergamon press, Oxford, New York, Seoul, Tokyo, 1993) 6th ed.

[25] Johanssen, A. *Manual of Petrographic Methods* (McGraw-Hill, New York, 1918).

[26] Usson, Y., Parazza, F., Jouk, P. S. and Michalowicz, G. (1994). Method for the study of the three-dimensional orientation of myocardial cells by means of confocal scanning laser microscopy, *Journal of Microscopy*, **174**, 101–110.

[27] Peskin, C. S. *Fiber architecture of the left venticle*, (unpublished lecture notes, Courant Institutes of Mathematical science, 1980).

[28] Spencer, A. J. M. *Continuum theory of the mechanics of fibre-reinforced composites*, (Springer-Verlag, 1984).

[29] Kevorkian, J. and Cole, J. D. *Perturbation methods in applied mathematics*, (Springer-Verlag, 1981).

[30] Ibarra-Polo, A. A., Guiloff, E. and Gomez-Rogers, C. (1972). Fetal heart rate throughout pregnancy, *Journal Obstetric Gynecology*, **113**, 814–818.

[31] Schmidt, K. G., Silverman, N. H. and Hoffman, J. I. E. (1995). Determination of ventricular volumes in human fetal hearts by two-dimensional echocardiography, *The American Journal of Cardiology*, **76**, 1313–1316.

[32] McCaffrey, F. M. and Sherman, F. S. (1997). Prenatal diagnosis of severe aortic stenosis, *Pediatric Cardiology*, **18**, 276–281.

[33] Demer, L. and Yin, F. C. P. (1983). Passive biaxial mechanical properties of isolated canine myocardium, *Journal of Physiology (London)*, **339**, 615–630.

[34] Pinto, J. G. (1987). A constitutive description of contracting papillary muscle and its implications to the dynamics of the intact heart, *Journal of Biomechanical Engineering*, **109**, 181–191.

[35] Friedman, W. F. (1972). The intrinsic physiologic properties of the developing heart, *Progress in Cardiovascular Diseases*, **15**, 87–111.

[36] Borg, T. K., Nakagawa, M., Carver, W. and Terracio, L. (1995). Overview: Extracellular matrix, receptors, and heart development. In *Developmental Mechanisms of Heart Disease* (eds. E. B. Clark, R. R. Markwald and A. Takao), Futura Publishing Company, 175–184.

[37] Hanson, M. A. (1993). The control of heart rate and blood pressure in the fetus: theoretical consideration. In *Fetus and Neonate Physiology and Clinical Applications: The Circulation* (eds. M. A. Hanson, J. A. D. Spencer and C. H. Rodeck), Cambridge university press, **1**, 1–22.

[38] Thornburg, K. L. and Morton, M. J. (1993). Growth and development of the heart. In *Fetus and Neonate Physiology and Clinical Applications: The Circulation* (eds. M. A. Hanson, J. A. D. Spencer and C. H. Rodeck), Cambridge university press, **1**, 137–159.

[39] Bovendeerd, P. H. M., Arts, T., Huyghe, J. M., Van Campen, D. H. and Reneman, R. S. (1992). Dependence of local left ventricular wall mechanics on myocardial fiber orientation: a model study, *Journal of Biomechanics*, **25:10**, 1129–1140.

[40] LeGrice, I. J., Takayama, Y. and Covell, J. W. (1995). Transverse shear along myocardial cleavage planes provides a mechanism for normal systolic wall thickning, *Circulation Research*, **77**, 182–193.

[41] Young, A. A., Imai, H., Chang, C. N. and Axel, L. (1993). Two-dimensional left ventricular deformation during systole using magnetic resonance imaging with spatial modulation of magnetization, *Circulation*, **89**, 740–752.

[42] Taber, L. A., Hu, N., Pexieder, T., Clark, E. B. and Keller, B. B. (1993). Residual strain in the ventricle of the stage 16–24 chick embryo, *Circulation Research*, **72**, 455–462.

[43] Rodriguez, E. K., Omens, J. H., Waldman, L. K. and McCulloch, A. D. (1993). Effect of residual stress on transmural sarcomere length distributions in rat left ventricle, *American Journal of Physiology*, **264**, H1048–H1056.

[44] Walker, A. M. (1993). Circulatory transitions at birth and the control of the neonatal circulation. In *Fetus and Neonate Physiology and Clinical Applications: The Circulation* (eds. M. A. Hanson, J. A. D. Spencer and C. H. Rodeck), Cambridge university press, **1**, 160–196.

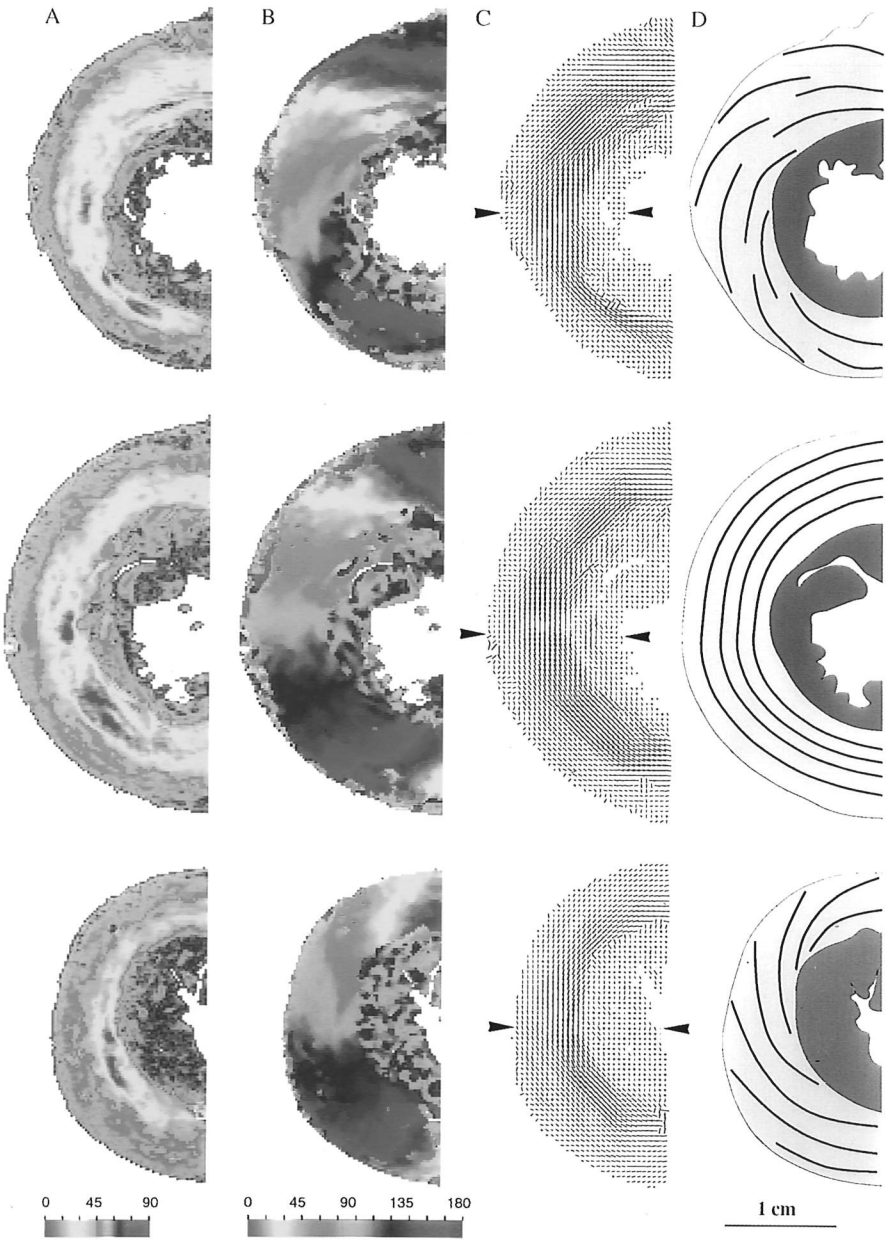

COLOUR PLATE I (see page 87, figure 2) Measured fibre organization in the lateral wall of the left ventricle on three transversal sections at the base (Top maps), the equator (middle maps) and the apex (Bottom maps) of the fetal heart of 33 weeks of gestational age (FH33). **Column A:** Colour maps giving the spatial distributions of the elevation angle in the transversal sections (colour scale: $0° \leq \gamma_{ele} \leq 90°$). **Column B:** Colour maps giving the spatial distributions of the azimuth angle in the transversal sections (colour scale: $0° \leq \gamma_{azi} \leq 180°$). **Column C:** 3D maps of measured fibre orientation, the angle between the direction of a segment and the horizontal line indicates the azimuth angle, the length of a segment is proportional to the planar projection of the orientation vector. It is maximal for a circular fibre (fibre running in the plane of the map) and minimal for a fibre orthogonal to the plane (crosses correspond to fibre whose elevation is superior to 60°). Arrows indicate the East-West axis in the lateral wall where the measurements are made. **Column D:** schematic drawing of the bundles of fibres as interpreted from the orientation maps. In the basal section, the bundles seem to radiate from endocardium to epicardium in an anticlockwise twisted fashion. At the equator the fibres are mainly circular and seem to follow perfectly the bow of the ventricular wall. At the apex, the bundles of fibres seem to radiate from endocardium to epicardium in an clockwise twisted fashion. Scale bar : 1 cm.

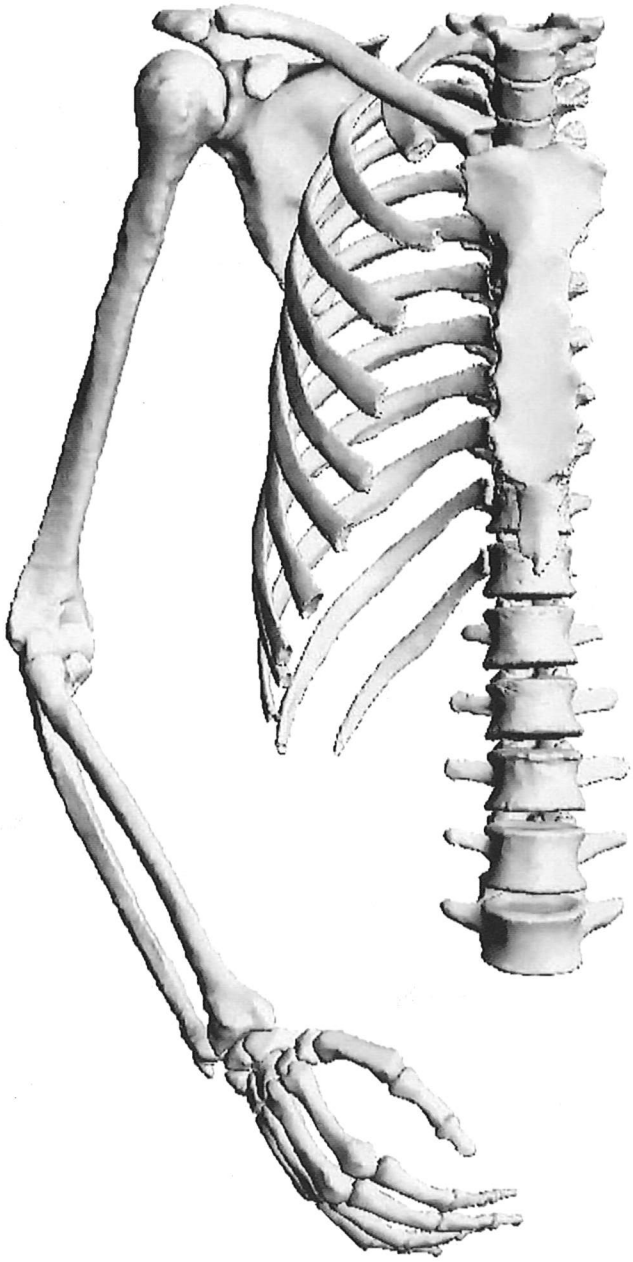

COLOUR PLATE II (see page 109, figure 1) Computer-generated rendering of the reconstructed bone surfaces used to develop the kinematic arm model. The three-dimensional bone surfaces were reconstructed from high-resolution, two-dimensional images of a human male cadaver obtained from the National Library of Medicine (see text). The bones are shown in the position of the cadaver when the images were made.